www.springer.com/41230
https://doi.org/10.1007/s41230-022-2031-0

Improvement in oxidation resistance of Cantor alloy through microstructure tailoring

Bao-lin Pang[1], Man Wang[1, 3], Yue-gang Shen[1], *Xiao-li Xi[1, 2], and Zuo-ren Nie[1, 2, 3]

1. Collaborative Innovation Center of Capital Resource-Recycling Material Technology, Faculty of Materials and Manufacturing, Beijing University of Technology, Beijing 100124, China

2. Key Laboratory of Advanced Functional Materials, Ministry of Education, Beijing University of Technology, Beijing 100124, China

3. National Engineering Laboratory for Industrial Big-data Application Technology, Beijing University of Technology, Beijing 100124, China

Abstract: A method of improving the oxidation resistance of Cantor alloy through microstructure tailoring was revealed. Samples with distinctive microstructures were achieved by different annealing treatments on the cold-rolled Cantor alloy. Oxidation test was then carried out on the various annealed samples at 800 °C for 24 h in air. The oxidation behavior was evaluated in terms of oxidation rate, surface and cross-section microstructure characterization. Although stratified oxide layers including outer Mn_2O_3 and inner Cr_2O_3 were observed in all the annealed samples, the thickness of Mn_2O_3 and Cr_2O_3 layers was different. Also, the samples exhibited different oxidation rates. The results indicate that the oxidation resistance of various annealed samples is closely related with grain size as well as twin density.

Keywords: Cantor alloy; annealing temperature; grain size; twins; oxidation behavior

CLC numbers: TG146.1+6; Document code: A; Article ID: 1672-6421(2022)06-503-08

***Xiao-li Xi**

Born in 1975, Ph. D, Professor. Her research interests include efficient separation and high-performance reconstruction of secondary metal resources, molten salt electrochemistry and its application, simulation of metallurgical process and fabrication and characterization of refractory alloys with high performance. To date, she has published more than 80 SCI indexed papers.

E-mail: xixiaoli@bjut.edu.cn

Received: 2022-02-25
Accepted: 2022-07-28

1 Introduction

The equiatomic CoCrFeMnNi high-entropy alloy (HEA), namely Cantor alloy, was firstly proposed by British Professor Cantor in 2004 [1, 2], which has become one of the most widely studied HEAs. Research works concerning mechanical properties, microstructure stability, high temperature resistance and radiation resistance of Cantor alloy have been widely carried out. Cantor alloy exhibits exceptional damage tolerance with fracture toughness exceeding 200 MPa·$m^{1/2}$ at cryogenic temperature, which is contributed to a transition from dislocation activity at room temperature to formation of mechanical nano-twinning with decreasing temperature [3]. He et al. [4] reported the phenomenon of microstructure instability in Cantor alloy, where Mn and Cr enriched precipitates were observed with low strain rates at elevated temperatures. It was also found that severe plastic deformation contributed to the formation of precipitates including NiMn, Cr-rich σ phase and FeCo during isothermal heat treatment at 450 °C [5]. Moreover, precipitates of Cr-rich σ phase and $M_{23}C_6$ during long-term annealing at 700 °C were confirmed by researchers. However, Cantor alloy exhibits stable microstructure without any precipitates above 800 °C [6-8]. Furthermore, it was found that the void size and swelling rate of the alloy increased significantly with the increase of irradiation temperature from 420 °C to 580 °C, but the swelling rate at 580 °C was still less than 0.4%, indicating that Cantor alloy has good irradiation swelling resistance [9].

Oxidation resistance is another important indicator of Cantor alloy especially at high temperature environment. Scholars have studied the oxidation behavior of Cantor alloy at high temperatures. Laplanche et al. [10] reported the oxidation rate (k) of Cantor alloy increased from 1.9×10^{-17} $m^2\cdot s^{-1}$ to 2.1×10^{-15} $m^2\cdot s^{-1}$ when the temperature increases from 600 °C to 900 °C. The high oxidation rate of Cantor alloy was related to fast outward

diffusion of Mn, which resulted in formation of pores and the number of pores increased with increasing oxidation temperature. Moreover, the vapor transport of pores accelerated the growth of Mn-rich oxide layer in turn. In addition, the oxide layer delaminated, including Mn_2O_3 and Mn_3O_4 in the outer layer and Cr_2O_3 in the inner layer. Kim et al. [11] studied the oxidation behavior of Cantor alloy at higher temperature ranging from 900 to 1,100 °C, where the weight gain increased from 1.76 to 9.08 mg·cm^{-2} with increasing oxidation temperature. The oxide layers were also inner Cr_2O_3 and outer Mn_2O_3 at 900 °C, while the outer layer transformed to $(Mn, Cr)_3O_4$ above 1,000 °C. Based on the research results mentioned above, it can be concluded that the oxidation resistance of Cantor alloy is inferior at relatively high temperatures, which is mainly due to the high diffusion rate of Mn and the consequent formation of loose Mn-containing oxide layer.

To avoid the negative influence of Mn on oxidation resistance, CoCrFeNi alloy without Mn was prepared and studied [12, 13]. However, Mn plays an important role in the mechanical properties of Cantor alloy. The addition of Mn can reduce stacking fault energy and consequently contribute to the formation of twins, thus improving both the strength and toughness of Cantor alloys [14]. Therefore, it is unwise to improve the oxidation resistance of Cantor alloy by removing Mn. Ye et al. [15] investigated the improvement of oxidation resistance of Cantor alloy at high temperature by adding Al with different contents. The results showed that the oxidation resistance of Al_xCoCrFeMnNi (x=0, 0.5, 1.0, 1.5, 2.0) high-entropy alloys increases with the increase of Al content. This is ascribed to the formation of dense Al_2O_3 and Cr_2O_3 oxide layers on the surface, which effectively hinders the outward diffusion of metal ions and inward diffusion of external oxygen. However, it is easy to produce dual phase of FCC and BCC when the Al content exceeds 0.8at.% [16, 17], which would weaken the mechanical and corrosion properties of the alloy.

Based on the above analysis, the oxidation resistance of Cantor alloys at high temperature is improved mainly through alloying method. While, microstructure is also critical to oxidation behavior of alloys apart from the alloying elements. In this study, the potential of improvement in oxidation resistance at 800 °C, a typical service temperature of Cantor alloy, was investigated through microstructure tailoring, i.e., the cold-rolled Cantor alloy was annealed at different temperatures for 1 h to obtain samples with different microstructures such as grain size and twins. Then, the effect of microstructure on oxidation behavior and mechanical properties of Cantor alloy, as well as the mechanise, was studied.

2 Experimental procedures

2.1 Sample preparation

Cantor alloy with mass of 2 kg was prepared by vacuum arc melting and copper mold casting. Due to the high vapor pressure of Mn, additional 5% of Mn was added to compensate for its evaporation during melting. In addition, the ingot was remelted for 5 times to ensure uniformity of chemical composition of the alloy. Moreover, the ingot was homogenized for 24 h at 1,200 °C to minimize segregation. After homogenization, the ingot was rolled at room temperature with a total reduction ratio of 95%, and then annealed at 700 °C, 800 °C and 900 °C for 1 h in a tube furnace under argon atmosphere, because the recrystallization temperature of Cantor alloy has been reported to be around 650 °C by different researchers [18-20]. The samples annealed at 700 °C, 800 °C and 900 °C were referred as S-700, S-800 and S-900 hereafter, respectively.

2.2 Oxidation test

The Cantor alloys annealed at different temperatures were cut into cuboids of 10 mm×10 mm×1 mm using a wire cutting machine. Prior to the oxidation test, all the surfaces of samples were mechanical polished with silicon carbide papers, and then mirror polished with 1 μm diamond suspension. The samples were cleaned with alcohol using ultrasonic cleaning and then dried using drying oven. The oxidation experiment was carried out at 800 °C for 24 h in air using a muffle furnace. To avoid its contact with the crucible during oxidation, the sample was suspended in an alumina crucible. When the oxidation test was completed, the crucible was taken out and cooled naturally in the air. Three samples were used for each condition and the average value was recorded.

2.3 Microstructure characterization

Chemical composition of the alloy was tested by X-ray fluorescence spectroscopy (XRF, ZSX Primus II). The contents of Cr, Mn, Fe, Co, and Ni were 19.95, 20.01, 19.77, 19.20 and 21.25 (at.%), respectively, all of which were close to the designed composition of 20at.%. Combustion method was adopted to analyze the impurity elements, and the results showed that the alloy contained 0.020at.% C, 0.004at.% O, 0.004at.% N and 0.008at.% S. X-ray diffractometer (XRD, D8 Advance) with Cu Kα radiation was used to analyze the phases before and after oxidation with a step size of 0.02°. The microstructure of cold-rolled and annealed Cantor alloys was observed by electron back-scattered diffraction (EBSD, Gemini SEM 300). In this process, the interpretation of EBSD data was carried out using orientation imaging microscopy (OIM, TexSEM). Measurement of grain size was performed using a linear intercept method according to ASTM E112. The surface morphology and composition of the oxidized samples were characterized by scanning electron microscopy (SEM, SU8020) equipped with energy dispersive spectrometer (EDS). To investigate the composition change of oxide layers with thickness, the cross section of oxidized samples was also analyzed using line EDS. Mass changes before and after oxidation were weighed using a a precision electronic balance.

3 Results

3.1 Microstructure evolution during annealing at different temperatures

Figure 1 shows XRD results of samples before and after annealing at different temperatures. It can be seen that all the

samples maintain a single FCC structure without precipitation of second phases. The diffraction peaks of the cold rolled sample are relatively broad, which is resulted from the introduced strain during cold rolling. Compared with the cold-rolled sample, the intensity of diffraction peak corresponding to (111) decreases while intensity of diffraction peaks of (200) and (220) increases in all the annealed samples. Also, the changing trend is enhanced with the increasing annealing temperature.

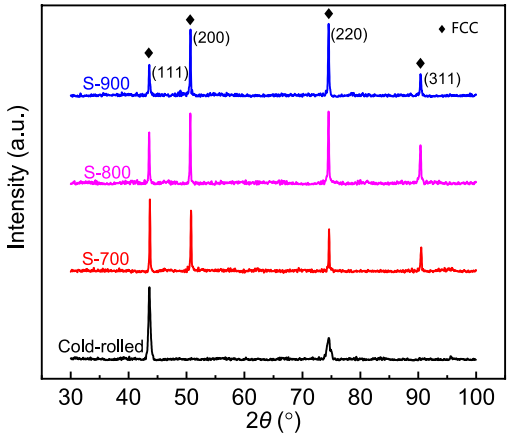

Fig. 1: XRD results of cold-rolled and annealed Cantor alloys

Figure 2 shows the EBSD results of cold-rolled and annealed samples. According to the inverse pole figure (IPF) shown in Fig. 2(a), the cold-rolled sample exhibits typical deformation microstructure, where the grains are mainly elongated along the rolling direction. Also, a preferred orientation texture of (111) is observed in the cold-rolled sample, which is consistent with the XRD results shown in Fig. 1. Compared with the elongated grains of cold-rolled sample, all the annealed samples experienced recrystallization and exhibit equiaxed grains, as shown in Figs. 2(b–d). The grains obviously grows with the increasing annealing temperature. The gain size of S-700, S-800 and S-900 is 1.84±0.36, 25.77±3.57 and 40.55±5.76 μm, respectively, as shown in Table 1. Moreover, annealing twins with a fraction of 42.8% are observed in the S-700. The fraction of twins further increases to 48.3% and 54.1% in S-800 and S-900, respectively. Therefore, samples with different microstructural characteristics were obtained through annealing treatments.

Figure 3 presents the tensile engineering stress-strain curves of cold-rolled and annealed samples tested at room temperature. The ultimate tensile strength (UTS) of cold-rolled sample reaches 1,117 MPa without yielding, indicating severe deterioration of ductility. Decent combination of strength and ductility was achieved through annealing treatments. For example, the yield strength (YS) and fracture elongation (EL) of S-700 are 416 MPa

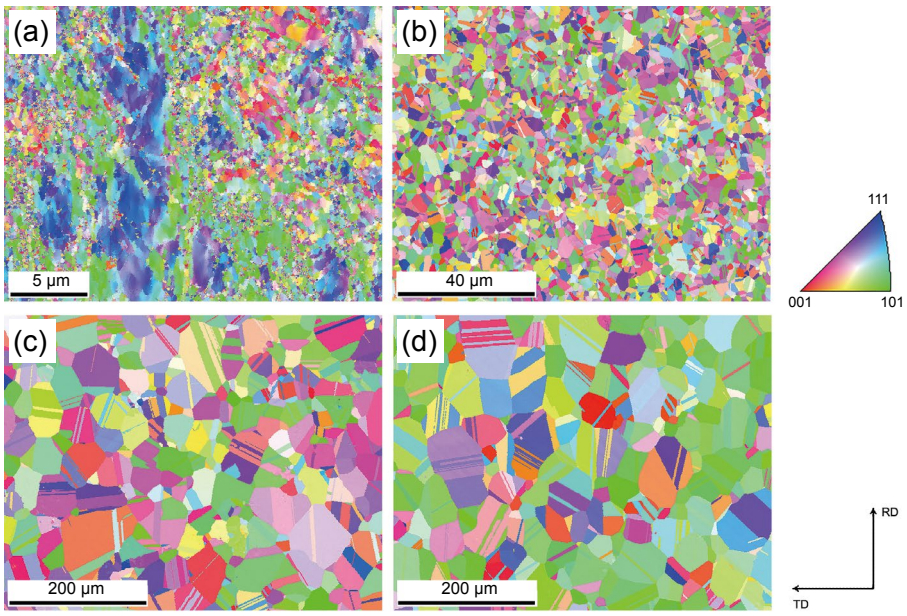

Fig. 2: EBSD results of cold-rolled and annealed Cantor alloys: (a) cold-rolled; (b) S-700; (c) S-800; (d) S-900

Table 1: Grain size and twin fraction of cold-rolled and annealed Cantor alloys

Sample	Grain size (μm)	Twin fraction (%)
Cold-rolled	0.29±0.11	0.35
S-700	1.84±0.36	42.8
S-800	25.77±3.57	48.3
S-900	40.55±5.76	54.1

and 37.5%, respectively. Although the tensile strength exhibits decrease with increasing annealing temperature, the ductility is further improved. It should be noted that the yield strength of S-900 is still higher than 200 MPa, which satisfies the basic requirement for engineering applications.

3.2 Oxidation behavior of different annealed samples

To quantitatively evaluate the oxidation resistance of annealed Cantor alloys, the oxidation rate k was calculated, which can

be expressed by Eq. (1):

$$k = \frac{\Delta m}{S * t} \quad (1)$$

where Δm, S and t represent the increase in oxidation weight, area and time, respectively. The oxidation rates of S-700, S-800 and S-900 are 1.2174, 1.2332 and 1.1913 g·(m^2·h)$^{-1}$, respectively. The annealed samples show different oxidation rates, which may be related with their distinctive microstructures.

Figure 4 shows the XRD results of annealed Cantor alloys after oxidation at 800 °C for 24 h. Mixed oxides of Mn_2O_3 and Cr_2O_3 were identified in all the three annealed samples after oxidation. Moreover, the Mn-rich oxide was dominated according to the relative intensity of diffraction peaks.

Figure 5 shows the SEM images of the surface morphologies after oxidation at 800 °C for 24 h. The surfaces of all the three

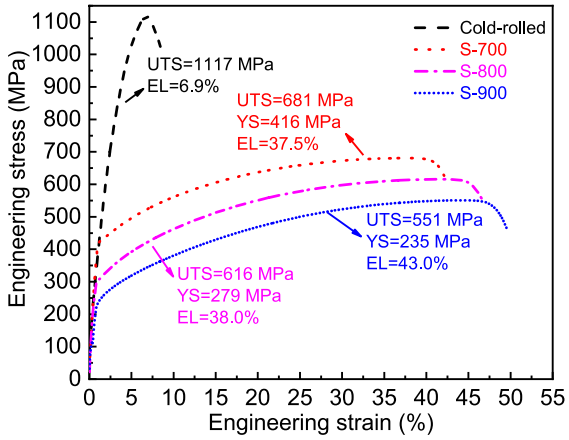

Fig. 3: Tensile engineering stress-strain curves of cold-rolled and annealed Cantor alloys tested at room temperature

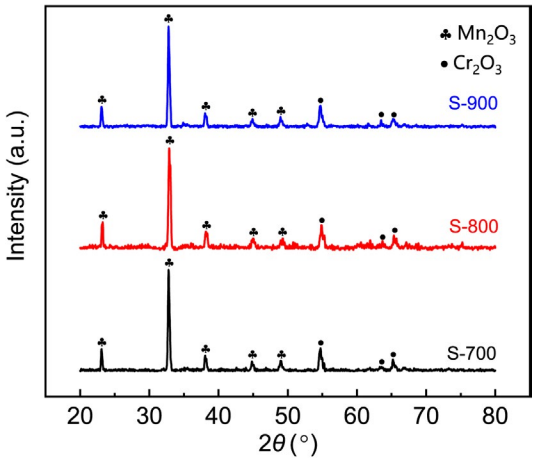

Fig. 4: XRD results of annealed Cantor alloys after oxidation at 800 °C for 24 h

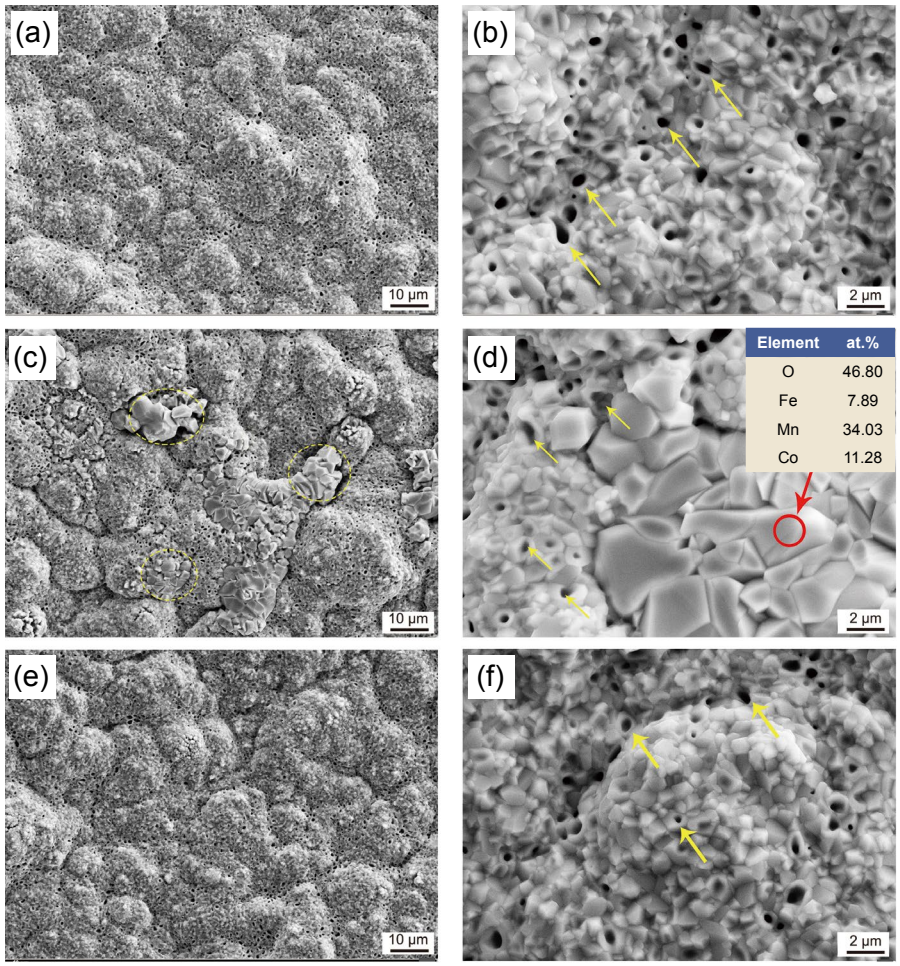

Fig. 5: SEM images of surface morphology of annealed Cantor alloys after oxidation at 800 °C for 24 h: (a, b) S-700; (c, d); S-800; (e, f) S-900

samples are covered with interconnected bumps, as shown in Figs. 5(a, c, e), where the size of bumps in S-800 and S-900 is relatively larger than those in S-700. According to the SEM images with higher amplification shown in Figs. 5(b, d, f), these bumps are made up of fine granular oxides. It should be noted that another kind of granular oxides with large size are also observed in S-800 as indicated by the dashed circles in Fig. 5(c), which maybe Mn_3O_4 based on the EDS results. In addition, there are many pores distributed on the surface of S-700 as indicated by the arrows in Fig. 5(b), which demonstrates that the oxide scale is loose. Compared with S-700, the number of pores decreases in the case of S-800 [Fig. 5(d)]. More importantly, the number of pores is siginificantly reduced on the surface of S-900, as shown in Fig. 5(f). Therefore, it can be summarized that the oxide scale formed in S-900 is the most dense, which is consistent with its lowest oxidation rate among the three samples.

Figures 6–8 depict the cross-section results of the three annealed samples after oxidation at 800 °C for 24 h. As shown in Figs. 6–8, the thickness of oxide scale in S-700, S-800 and S-900 is 13.25, 8.13 and 7.13 μm, respectively. According to the EDS mapping results, the oxide scales are stratified into the outer Mn-rich layer and inner Cr-rich layer in all the three samples. Combined with XRD results, it can be reasonably claimed that the outer layer is Mn_2O_3 and the inner layer is Cr_2O_3. Besides, the internal and external oxide layers are partially overlapped according to the mapping results in Figs. 6–8. Moreover, the thickness of inner and outer layer in different samples is varied based on the EDS line results given in Figs. 6(b), 7(b) and 8(b). The total thickness of oxide layer is slightly smaller than the additive thickness of inner and outer layers in all the three samples due to overlap of the stratified layers. It should be noted that the thickness of inner Cr_2O_3 layer in S-700 is 3.50 μm and decreases to 3.13 μm in S-800, while increases to 4.38 μm in S-900. However, the thickness of outer Mn_2O_3 layer shows an inverse decreasing trend in the sequence of S-700, S-800 and S-900.

Apart from the stratified oxide layers, there is a porous zone beneath the oxide scale in both S-700 [Fig. 6(a)] and S-800 [Fig. 7(a)]. The pores were confirmed to be kirkendall pores, which was also reported and ascribed to the fast diffusion of Mn in Ref. [12]. In this study, it seems that the porous zone is also closely related with the Mn-depleted zone according to Mn-mapping results shown in Figs. 6–8. The porous zone has a thickness of 25.38 μm in S-700, but decreases to 12.53 μm in S-800. It should be noted that the porous zone is only 7.25 μm in thickness in the case of S-900, and the number of pores also significantly decreases.

4 Discussion

4.1 Microstructure characteristics of annealed samples

According to the XRD and EBSD results shown in Figs. 1 and 2, (111) texture exists in the cold rolled Cantor alloy, which is commonly found in plastically deformed face-centered high-entropy alloys [21]. The microstructure evolution during annealing shown in Fig. 2 indicates that equiaxed grains was achieved in all the three annealed samples because of recrystallization, and grain growth was observed with the

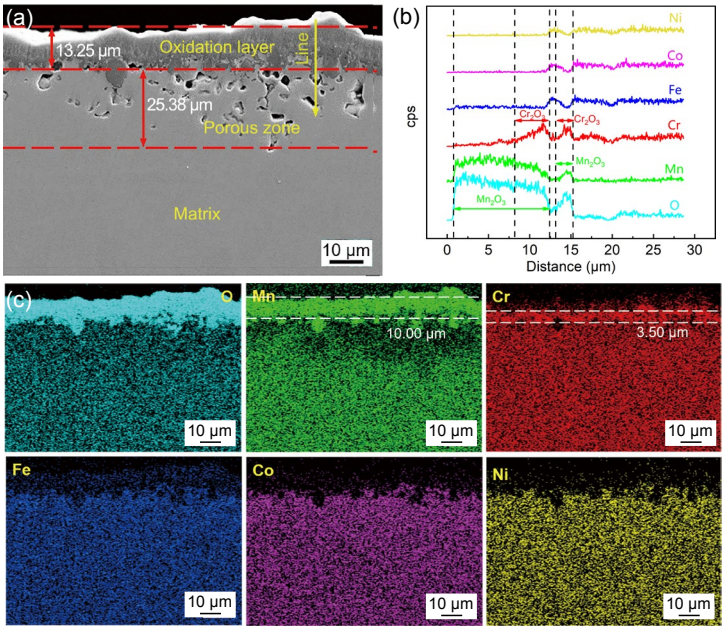

Fig. 6: Cross section results of S-700 after oxidation at 800 °C for 24 h: (a) cross section morphology; (b) EDS line results corresponding to the yellow line marked in (a); (c) mapping results of the oxide scale corresponding to (a)

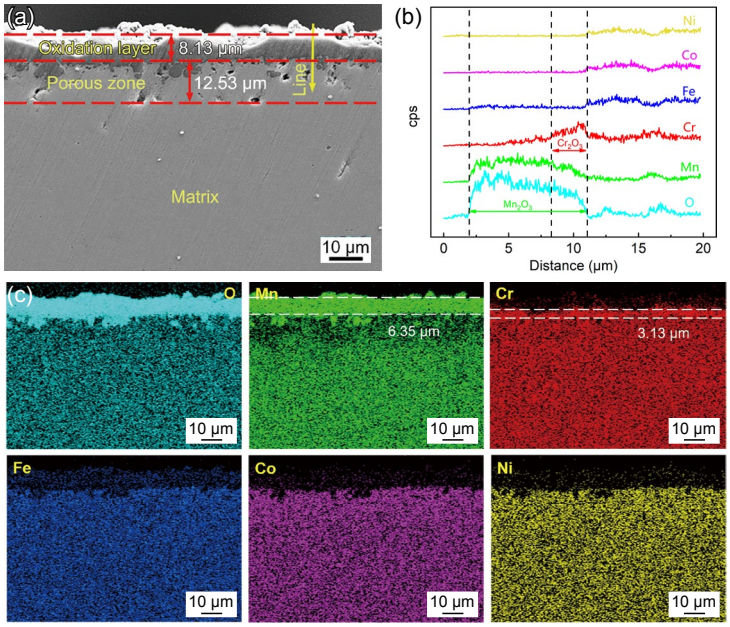

Fig. 7: Cross section results of S-800 after oxidation at 800 °C for 24 h: (a) cross section morphology; (b) EDS line results corresponding to the yellow line marked in (a); (c) mapping results of the oxide scale corresponding to (a)

increasing annealing temperature. Thus, the intensity of diffraction peak corresponding to (111) texture decreases with the increasing annealing temperature. As shown in Table 1, the grain size of S-700, S-800 and S-900 increases to 1.84 μm, 25.77 μm and 40.55 μm, respectively. Furthermore, annealing twins with an increasing fraction are identified in the annealed samples, which are ascribed to the low stacking fault energy of Cantor alloy [22-25]. Compared with the cold-rolled sample, the twin fraction of S-700, S-800 and S-900 increases from 0.35% to 42.8%, 48.3% and 54.1%, respectively. Therefore, samples with different microstructural characteristics can be obtained through annealing treatments, and detailed results are summarized in Table 1.

4.2 Effects of microstructure on oxidation behavior

The three annealed samples with distinctive microstructure were then oxidized at 800 °C for 24 h, and the oxidation results are listed in Table 2. It can be seen that the S-900 has the lowest oxidation rate of 1.1913 $g\cdot(m^2\cdot h)^{-1}$, while S-800 has the highest oxidation rate of 1.2332 $g\cdot(m^2\cdot h)^{-1}$. Stratified oxide layers including outer Mn_2O_3 and inner Cr_2O_3 are observed in all the three samples. The total thickness of oxide layer decreases obviously with the increase of annealing temperature. The thickness of the outer Mn_2O_3 layer shows the same decreasing trend with the total thickness. However, there is a transition in the thickness of inner Cr_2O_3 layer for the annealed samples, where it decreases from 3.50 μm in S-700 to 3.13 μm in S-800 while increases to 4.38 μm in S-900. In addition, obvious porous zones with thickness of 25.38 and 12.53 μm are observed beneath the oxide scale in S-700 and S-800 (Figs. 6–7), respectively. It is worth noting that the porous zone is significantly reduced to 7.25 μm and only several pores with finer size are observed in S-900 (Fig. 8). In summary, S-900 exhibits the best oxidation resistance among the three annealed samples, which may be related to its coarser grain size and higher twin fraction.

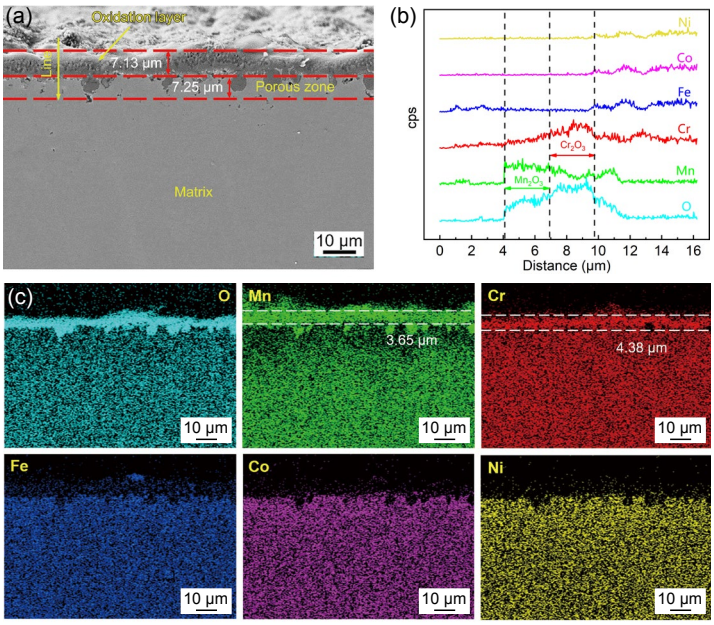

Fig. 8: Cross section results of S-900 after oxidation at 800 °C for 24 h: (a) cross section morphology; (b) EDS line results corresponding to the yellow line marked in (a); (c) mapping results of the oxide scale corresponding to (a)

Stratified oxide layer including outer Mn-rich and inner Cr-rich layers is a widely reported oxidation phenomenon [10, 11], which is closely related with the respective diffusion rate of multi-principal elements in Cantor alloy. According to the research results reported by Tsai et al. [26] and Kai et al. [27], the element sequence in decreasing diffusion rate is as following: Mn>Cr>Fe>Co>Ni. Then, Mn and Cr would preferentially diffuse outward and get oxidized on the surface of specimens. It has been reported that Cr_2O_3 is the only stable phase in Cr-O system, while four stable oxides including MnO, Mn_3O_4, Mn_2O_3 and MnO_2 exist in the Mn-O system [28, 29]. Among the Mn-rich oxides, Mn_2O_3 could keep stable up to 877 °C [30]. Therefore, mixed Mn_2O_3 and Cr_2O_3 were identified based on the XRD (Fig. 4) and EDS mapping (Figs. 6–8) results, since the oxidation test was carried out at 800 °C for 24 h in this study. Further, Mn exhibits relatively higher diffusion rate than that of Cr, and consequently the formed Mn_2O_3 constitutes the outer layer of stratified oxide layer, which is consistent with the mapping results shown in Figs. 6–8. In addition, the outer Mn_2O_3 layer is relatively thick, which makes it difficult to identify the inner Cr_2O_3 layer using XRD, resulting in the lower intensity of diffraction peaks corresponding to Cr_2O_3, as shown in Fig. 4.

The surface morphology of oxide layers shown in Figs. 5(a, c, e) indicates that the size of bumps increase in the sequence of S-700, S-800 and S-900. This is related to the grain size of annealed samples, as grain boundaries (GBs) are fast diffusion channels for metals and oxygen [31]. The annealed samples experience recrystallization as well as grain growth with the

Table 2: Oxidation results of different annealed samples after oxidation at 800 °C for 24 h

Sample	Oxidation rate $g\cdot(m^2\cdot h)^{-1}$	Oxidation layer (μm)			Porous zone (μm)
		Total thickness	Outer Mn_2O_3	Inner Cr_2O_3	
S-700	1.2174	13.25	10.00	3.50	25.38
S-800	1.2332	8.13	6.35	3.13	12.53
S-900	1.1913	7.13	3.65	4.38	7.25

increased annealing temperature (Fig. 2), giving grain size of 1.84, 25.77, 40.55 μm for S-700, S-800 and S-900, respectively. Then, Mn and Cr have the maximum channels for outward diffusion in the case of S-700, and the largest number of GBs also provide more nucleation sites for oxidation, leading to the smallest bump size of surface oxide layers. Therefore, the thickness of outer Mn_2O_3 layer is the largest in the case of S-700, followed by S-800. In addition, the out Mn_2O_3 layer is loose, which is demonstrated by the dense pores distributed on the surface of oxide layers [Figs. 5(b) and (d)]. Then, it can be inferred that this loose outer Mn_2O_3 layer provides paths for inward diffusion of oxygen and results in continuous oxidation.

Contrary to the outer Mn_2O_3 layer, there is a transition in the thickness of inner Cr_2O_3 layer in S-800. It decreases from 3.50 μm in S-700 to 3.13 μm in S-800 while increases to 4.38 μm in S-900. The inner Cr_2O_3 layer is more compact than that of outer Mn_2O_3 layer, thus giving more effective oxidation resistance. Then, it can be reasonably inferred that the decreased Cr_2O_3 layer thickness in S-800 would cause more Mn diffusion outward, leading to the formation of Mn_3O_4 as indicated by the red arrow in Fig. 5(d). The reaction can be expressed by the following:

$$2Mn+2Mn_2O_3+O_2 \rightarrow 2M_3O_4 \quad (2)$$

The Mn_3O_4 only appears in S-800, indicating that the change of oxide layer is not only related to the number of grain boundaries, but also related to other diffusion channels, such as twin boundaries. Compared with S-700 and S-800, S-900 contains the highest fraction of twins, around 54.1%. Holcomb et al. [32] reported that twin boundaries assists precipitation of Cr-rich σ phase in a non-equiatomic high-entropy alloy ($Fe_{32}Co_{20}Mn_{18}Cr_{15}Ni_{15}$), indicating that twin boundaries are more favorable diffusion paths for Cr. Similar effect of twin boundaries was also reported in nickel alloy [33]. In this study, it can be reasonably assumed that the higher twin density supplies more diffusion paths for Cr, which may promote the formation of continuous Cr_2O_3 layer. The varied thickness of Cr_2O_3 layer indicates that the formation of Cr_2O_3 layer is not only dependent on the number of grain boundary, but also the fraction of twin boundaries. Besides, it can be found that kirkendall pores appear beneath the oxide layer of different annealed samples, among which S-700 sample is the most, followed by S-800. The formation of kirkendall pores is caused by the rapid outward diffusion of Cr and Mn elements. These pores would accelerate the growth of oxide layer in turn as they provide a short circuit path for diffusion [34, 35]. Therefore, S-900 exhibits the lowest oxidation rate and best oxidation resistance among the three samples.

5 Conclusions

The oxidation behavior of Cantor alloys with different microstructures tested at 800 °C for 24 h was investigated. The following conclusions can be drawn:

(1) The grain size and fraction of twins increase with the increasing annealing temperature. The grain size and twin fraction of samples annealed at 700 °C, 800 °C and 900 °C are 1.84 μm, 25.77 μm, 40.55 μm and 42.8%, 48.3%, 54.1%, respectively.

(2) Stratified oxide scales including outer Mn_2O_3 and inner Cr_2O_3 are observed in all the three samples after oxidation at 800 °C for 24 h, which are resulted from the relative faster diffusion rates of Mn and Cr than the other principal elements in Cantor alloy.

(3) The outward diffusion of Mn is suppressed by increasing grain size, resulting in reduction in the thickness of loose outer Mn_2O_3 layer. Besides, increased number of twins can accelerate the diffusion of Cr, leading to the formation of protective Cr_2O_3 layer. These two factors contribute to the best oxidation resistance of S-900 in terms of oxidation rate, surface and cross-section microstructure and thickness of oxide layer.

(4) Considering the effects of microstructure on oxidation behavior and mechanical properties, excellent comprehensive properties can be obtained by tailoring microstructure by annealed at different temperatures. This also provides a practical and powerful reference for the development of alloys.

Acknowledgements

This work was financially supported by the National Natural Science Foundation of China (Nos. 52025042, 51621003).

References

[1] Yeh J W, Chen S K, Lin S J, et al. Nanostructured high-entropy alloys with multiple principal elements: Novel alloy design concepts and outcomes. Advance Engineering Materials, 2004, 6(5): 299–303.
[2] Cantor B, Chang I T H, Knight P, et al. Microstructural development in equiatomic multicomponent alloys. Materials Science and Engineering: A, 2004, 375–377: 213–218.
[3] Gludovatz B, Hohenwarter A, Catoor D, et al. A fracture-resistant high-entropy alloy for cryogenic applications. Science, 2014, 345(6201): 1153–1158.
[4] He J Y, Zhu C, Zhou D Q, et al. Steady state flow of the FeCoNiCrMn high entropy alloy at elevated temperatures. Intermetallics, 2014, 55: 9–14.
[5] Schuh B, Mendez-Martin F, Völker B, et al. Mechanical properties, microstructure and thermal stability of a nanocrystalline CoCrFeMnNi high-entropy alloy after severe plastic deformation. Acta Materialia, 2015, 96: 258–268.
[6] Otto F, Dlouhý A, Pradeep K G, et al. Decomposition of the single-phase high-entropy alloy CrMnFeCoNi after prolonged anneals at intermediate temperatures. Acta Materialia, 2016, 112: 40–52.
[7] Stepanov N D, Shaysultanov D G, Ozerov M S, et al. Second phase formation in the CoCrFeNiMn high entropy alloy after recrystallization annealing. Materials Letters, 2016, 185: 1–4.
[8] Ye F X, Jiao Z P, Yang Y. Effect of medium temperature precipitation phase and Mn element diffusion mechanism on high temperature oxidation process of repair and remanufacture CoCrFeMnNi high-entropy alloy cladding. Materials Research Express, 2019, 6(5): 056521.
[9] Yang T N, Lu C, Velisa G, et al. Influence of irradiation temperature on void swelling in NiCoFeCrMn and NiCoFeCrPd. Scripta Materialia, 2019, 158: 57–61.

[10] Laplanche G, Volkert U F, Eggeler G, et al. Oxidation behavior of the CrMnFeCoNi high-entropy alloy. Oxidation of Metals, 2016, 85(5–6): 629–645.
[11] Kim Y K, Joo Y A, Kim H S, et al. High temperature oxidation behavior of Cr-Mn-Fe-Co-Ni high entropy alloy. Intermetallics, 2018, 98: 45–53.
[12] Yu X X, Taylor M A, Perepezko J H, et al. Competition between thermodynamics, kinetics and growth mode in the early-stage oxidation of an equimolar CoCrFeNi alloy. Acta Materialia, 2020, 196: 651–659.
[13] Doleker K M, Erdogan A, Zeytin S. Laser re-melting influence on isothermal oxidation behavior of electric current assisted sintered CoCrFeNi, CoCrFeNi$Al_{0.5}$ and CoCrFeNi$Ti_{0.5}Al_{0.5}$ high entropy alloys. Surface and Coatings Technology, 2021, 407: 126775–126786.
[14] Xiao H, Liu Y, Wang K, et al. Effects of Mn content on mechanical properties of FeCoCrNiMnx ($0 \le x \le 0.3$) high-entropy alloys: A first-principles study. Acta Metallurgica Sinica (English Letters), 2020, 34(4): 455–464.
[15] Ye F X, Jiao Z P, Yan S, et al. Microbeam plasma arc remanufacturing: Effects of Al on microstructure, wear resistance, corrosion resistance and high temperature oxidation resistance of Al_xCoCrFeMnNi high-entropy alloy cladding layer. Vacuum, 2020, 174(C): 109178.
[16] Kumar J, Kumar N, Das S, et al. Effect of Al addition on the microstructural evolution of equiatomic CoCrFeMnNi alloy. Transactions of the Indian Institute of Metals, 2018, 71(11): 2749–2758.
[17] He J Y, Liu W H, Wang H, et al. Effects of Al addition on structural evolution and tensile properties of the FeCoNiCrMn high-entropy alloy system. Acta Materialia, 2014, 62(1): 105–113.
[18] Bhattacharjee P P, Sathiaraj G D, Zaid M, et al. Microstructure and texture evolution during annealing of equiatomic CoCrFeMnNi high-entropy alloy. Journal of Alloys and Compounds, 2014, 587: 544–552.
[19] Abbasi E, Dehghani K. Hot tensile properties of CoCrFeMnNi(NbC) compositionally complex alloys. Materials Science & Engineering A, 2020, 772: 771–780.
[20] Jeong H T, Park H K, Park K, et al. High-temperature deformation mechanisms and processing maps of equiatomic CoCrFeMnNi high-entropy alloy. Materials Science and Engineering: A, 2019, 756: 528–537.
[21] Tang Q H, Huang Y, Cheng H, et al. The effect of grain size on the annealing-induced phase transformation in an $Al_{0.3}$CoCrFeNi high entropy alloy. Materials & Design, 2016, 105: 381–385.
[22] Randle V. Twinning-related grain boundary engineering. Acta Materialia, 2004, 52(14): 4067–4081.
[23] Kumar M, Schwartz A J, King W E. Microstructural evolution during grain boundary engineering of low to medium stacking fault energy fcc materials. Acta Materialia, 2002, 50(10): 2599–2612.
[24] Palumbo G, Lehockey E M, Lin P. Applications for grain boundary engineered materials. JOM, 1998, 50(2): 40–43.
[25] Haase C, Barrales-Mora L A, Molodov D A, et al. Texture evolution of a cold-rolled Fe-28Mn-0.28C TWIP steel during recrystallization. Materials Science Forum, 2013, 2379(753): 213–216.
[26] Tsai K Y, Tsai M H, Yeh J W. Sluggish diffusion in Co-Cr-Fe-Mn-Ni high-entropy alloys. Acta Materialia, 2013, 61(13): 4887–4897.
[27] Kai W, Li C C, Cheng F P, et al. The oxidation behavior of an equimolar FeCoNiCrMn high-entropy alloy at 950 °C in various oxygen-containing atmospheres. Corrosion Science, 2016, 108: 209–214.
[28] Enke C G. Nonstoichiometry, diffusion, and electrical conductivity in binary metal oxides. Materials and Corrosion, 1974, 25(10): 801–802.
[29] Hed A Z, Tannhauser D S. Contribution to the Mn-O phase diagram at high temperature. Journal of the Electrochemical Society, 2019, 114(4): 314–314.
[30] Speidel D H, Muan A. The system manganese oxide-Cr_2O_3 in air. Journal of the American Ceramic Society, 1963, 46(12): 577–578.
[31] Liu M, Kang Q J, Xu H W. Grain-scale study of the grain boundary effect on UO_2 fuel oxidation and fission gas release under reactor conditions. Chemical Engineering Science, 2021, 229: 116026.
[32] Holcomb G R, Tylczak J, Carney C. Oxidation of CoCrFeMnNi high entropy alloys. JOM, 2015, 67(10): 2326–2339.
[33] Jackson P R S, Wallwork G R. High temperature oxidation of iron-manganese-aluminum based alloys. Oxidation of Metals, 1984, 21(3–4): 135–170.
[34] Hou J H, Li J J, Lu W J. Twin boundary-assisted precipitation of sigma phase in a high-entropy alloy. Materials Letters, 2021, 300: 130198.
[35] Ma W B, Luo H Y, Yang X Q. The effects of grain size and twins density on high temperature oxidation behavior of nickel-based superalloy GH738. Materials (Basel), 2020, 13(18): 4166.